Improvement of Heat-Affected Zone Toughness of Steel Plates for High Heat Input Welding by Inclusion Control with Ca Deoxidation

Ruizhi Wang [1,2], Jian Yang [1,3],*, and Longyun Xu [3]

1   School of Metallurgy, Northeastern University, Shenyang 110083, China; wangruizhi@baosteel.com
2   Steelmaking Research Department, Research Institute, Baosteel Group Corporation, Shanghai 201900, China
3   State Key Lab of Advanced Special Steel, School of Materials Science and Engineering, Shanghai University, Shanghai 200444, China; xulongyun@shu.edu.cn
*   Correspondence: yang_jian@t.shu.edu.cn; Tel.: +86-021-3604-7721

check for updates

Abstract: The characteristics of inclusions and microstructure in heat-affected zones (HAZs) of steel plates with Ca deoxidation after high heat input welding of 400 kJ·cm^{-1} were investigated through simulated welding experiments and inclusions automatic analyzer systems. Typical inclusions in HAZs of steels containing 11 ppm and 27 ppm Ca were recognized as complex inclusions with the size in the range of 1~3 μm. They consisted of central Al_2O_3 and peripheral CaS + MnS with TiN distributing at the edge (Al_2O_3 + CaS + MnS + TiN). With increasing Ca content in steel, the average size of inclusions decreased from 2.23 to 1.46 μm, and the number density increased steadily from 33.7 to 45.0 mm^{-2}. Al_2O_3 + CaS + MnS + TiN complex inclusions were potent to induce the formation of intragranular acicular ferrite (IAF). Therefore, the HAZ toughness of steel plates after high heat input welding was improved significantly by utilizing oxide metallurgy technology with Ca deoxidation.

Keywords: heat-affected zone; high heat input welding; Ca deoxidation; inclusion control; intragranular acicular ferrite

1. Introduction

In recent years, the high heat input welding technology with the heat input larger than 400 kJ·cm^{-1} has been widely used for welding heavy steel plates in the areas of shipbuilding, architectural construction, etc. For example, the heat input of tandem electrogas welding could reach 500 kJ·cm^{-1}. Also, that this kind of welding process is applicable to a very limited portion of material, since the welding spot is very limited. During the high heat input welding process, the heat-affected zone (HAZ) of steel plate is exposure at temperatures as high as 1400 °C for a long time, with a relatively low cooling rate. As a consequence, the HAZ microstructure is coarsened, leading to a significant degradation of the HAZ toughness [1,2].

It is widely accepted that the oxide metallurgy technology is an effective method for the improvement of HAZ toughness of steel plates after high heat input welding [3]. Oxide metallurgy technology refers to oxide inclusions and other kinds of inclusions and precipitates, serving as nucleation sites of intragranular acicular ferrite (IAF) or pinning the growth of austenite grain during the welding process. Nowadays, it has been extensively studied to develop advanced oxide metallurgy technology utilizing strong deoxidizers, such as Mg and Zr. Yang et al. [1,4–6] have developed third-generation oxide metallurgy technology to obtain excellent HAZ toughness by inclusion control with Mg deoxidation. They found that the formation of micro-meter inclusions and the nano-meter precipitates in steel plates can effectively promote the formation of IAF and restrain the growth of γ

grains, respectively. Shi et al. [7] reported the excellent toughness (more than 100 J) of HAZ with the heat input of 400 kJ·cm^{-1} in Zr bearing low carbon steel, attributing to the proper austenite grain size that favored the development of IAF. Kojima et al. [8] reported that the HAZ toughness was improved significantly by using fine particles with sizes of 10–100 nm containing Mg or Ca.

Ca treatment is a well-established method to transform solid alumina clusters to liquid calcium aluminates in order to avoid nozzle clogging problems in continuous casting of Al-killed steels [9]. Although Ca is also a kind of strong deoxidizing element and is widely used in the area of inclusion modification, termed as Ca treatment, limited research on oxide metallurgy technology with Ca deoxidation has been reported [10–13]. In view of the advantages of steel industrial application of Ca, it has scientific and industrial values to investigate the oxide metallurgy technology by inclusion control with Ca deoxidation to improve the HAZ toughness.

In this paper, the characteristics of inclusions and microstructure in HAZs of steel plates with Ca deoxidation are studied after high heat input welding of 400 kJ·cm^{-1}. In addition, the mechanism of improvement of HAZ toughness after high-heat input welding by inclusion control with Ca deoxidation is illustrated.

2. Experimental Procedures

2.1. Experimental Steel Preparation

Steel samples were melted in a 50-kg vacuum induction furnace with sintered magnesia lining. Table 1 shows the major chemical compositions of experimental steel samples. The method for steel chemical analysis is Method for Photoelectric Emission Spectroscopic Analysis by JIS G 1253-2002. The measurement of C, O and N are Combustion and Melting Technology by ASTM E1019-11. As shown in Table 1, steel samples C11 and C27 were both prepared by oxide metallurgy technology with Ca deoxidation, which Ca contents were measured to be 11 and 27 ppm, respectively. For comparison, a conventional Al-killed steel without Ca deoxidation denoted as A was used in the present study. Deoxidation process was carried out in the furnace under the Ar atmosphere. About 40 kg of pure iron was first melted, and lime (CaO) was added as top slag to assure considerably low oxygen potential in slag. Proper amount of deoxidants of Mn, Si, Al, Ti and Ca was added in order to obtain the target steel compositions. The melt was then cast into an ingot with the size of 120 × 180 × 240 (mm^3), and each ingot was hot rolled into a steel plate with the thickness of 50 mm. Roughing rolling was conducted at the temperature above 930 °C with the reduction ratio larger than 30%, and finishing rolling was carried out at the temperature of about 800 °C with the reduction ratio larger than 30%. Subsequently, the steel plate was cooled down from 760 °C to 400 °C at the cooling rate of about 10 °C·s^{-1}.

Table 1. Chemical compositions of the experimental steels (wt%).

Steel	C	Mn	P	S	Ca	Al	Ti	O	N
A	0.078	1.5	0.01	0.005	0.0005	0.026	0.012	0.0022	0.0014
C11	0.078	1.5	0.01	0.005	0.0011	0.011	0.014	0.0012	0.0029
C27	0.078	1.5	0.01	0.005	0.0027	0.015	0.013	0.0013	0.0030

2.2. Welding Thermal Simulation Experiments

In order to evaluate the HAZ toughness of the experimental steel plates, simulated welding experiments were carried out by use of Gleeble 3800 (Dynamic Systems Inc., New York, NY, USA). It was designed to simulate an electrogas arc welding with the heat input of 400 kJ·cm^{-1} for the steel plate with a thickness of 50 mm. The steel sample for simulated welding experiments with the size of 11 × 11 × 55 (mm^3) was cut down from the position about 1/4 width and 1/4 length from the edge of steel plate. As shown in Figure 1, the peak welding temperature was 1400 °C with a holding time of 3 s. The cooling rates from 1400 to 800 °C, from 800 to 500 °C and from 500 to 300 °C were controlled

to be 3.41, 0.78, 0.17 $^\circ$C·s^{-1}, respectively. Then, the standard V notch Charpy impact tests of HAZs were conducted at $-20\ ^\circ$C for the samples after simulated welding experiments.
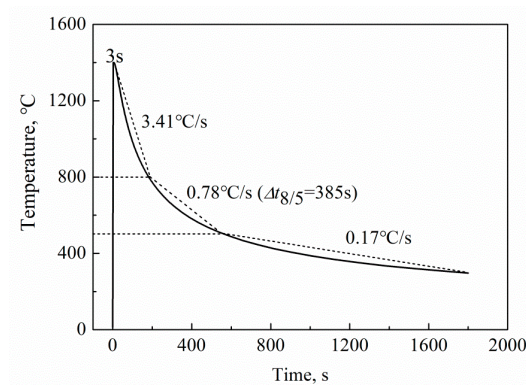

Figure 1. Thermal cycle of simulated heat-affected zone (HAZ) of high heat input welding with 400 kJ·cm^{-1}.

2.3. Characterization of Inclusions and Microstructures

These HAZ specimens were taken from the surfaces in parallel with the fracture cross sections after Charpy impact tests. Firstly, these specimens were polished and then analyzed by the inclusion automatic analyzer system (IAAS) made in Germany. IAAS is consisted of scanning electron microscope (SEM), energy-dispersive spectroscopy (EDS) and software which can analyze the inclusions automatically. Then HAZ specimens were etched by 4% nital to observe the HAZ microstructures with optical microscopy and SEM. The present study mainly focuses on the inclusions with the equal-circle size larger than 1 μm. The equal-circle size is given by the diameter of a circle whose area is equal to the area occupied by the inclusion in the SEM picture. Mapping scanning of typical inclusions in each sample was performed in order to determine the elemental distribution inside the inclusions. A schematic drawing with the sampling procedure is shown in Figure 2.
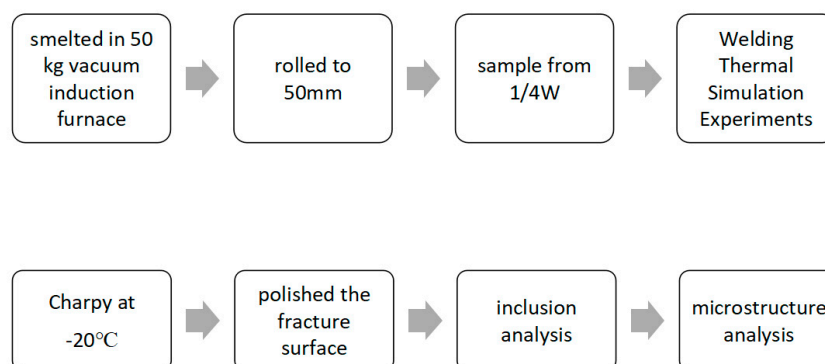

Figure 2. Schematic draw with the sampling procedure.

3. Results

3.1. HAZ Toughness

The Charpy impact test results of HAZs at $-20\ ^\circ$C of steel samples A, C11, and C27 are shown in Table 2. All three Charpy-absorbed energy values of steel sample A are very low with the average value of only 27 J. Obviously, the HAZ toughness of the conventional Al-killed steel of sample A without Ca deoxidation was greatly deteriorated after high heat input welding. The average Charpy-absorbed energy values of steel samples C11 and C27, both with Ca deoxidation, are 187 J and 123 J, respectively. By comparison, the HAZ toughness values of these two steel samples were increased by more than

four times. It is clear that excellent HAZ toughness of steel plate after high heat input welding with 400 kJ·cm^{-1} has been obtained by utilizing oxide metallurgy technology with Ca deoxidation.

Table 2. Charpy-absorbed energy of HAZ at $-20\ ^\circ$C.

Specimen	Individual Value (J)	Mean Value (J)	FA (%)	Standard Deviation
A	14, 33, 34	27	0, 5, 5	127
C11	180, 189, 192	187	70, 70, 70	39
C27	88, 136, 144	123	35, 45, 50	917

Figure 3 shows the macro fractographs and SEM images of the fracture surfaces of the HAZs in steel samples A, C11 and C27 after Charpy impact tests. The fractographs of steel samples C11 and C27 show the obvious transverse deformation, indicated by the lateral expansion or notch contraction as shown in Figure 3d,g. In contrast, steel sample A does not show any transverse deformation (Figure 3a). Figure 3b,c shows that the fracture surface of steel sample A is covered with radial zones and river-like patterns, indicating a brittle fracture and inferior HAZ toughness. The ratios of radial zones in fractures for steel samples C11 and C27 are less than that of steel sample A, as shown in Figure 3d,g. Both are full of fibrous zones containing large quantity of dimples, as shown in Figure 3e,f,h,i. It manifests that the HAZ fracture mode of steel samples C11 and C27 is ductile fracture. Thus, steel samples C11 and C27 show excellent HAZ toughness.
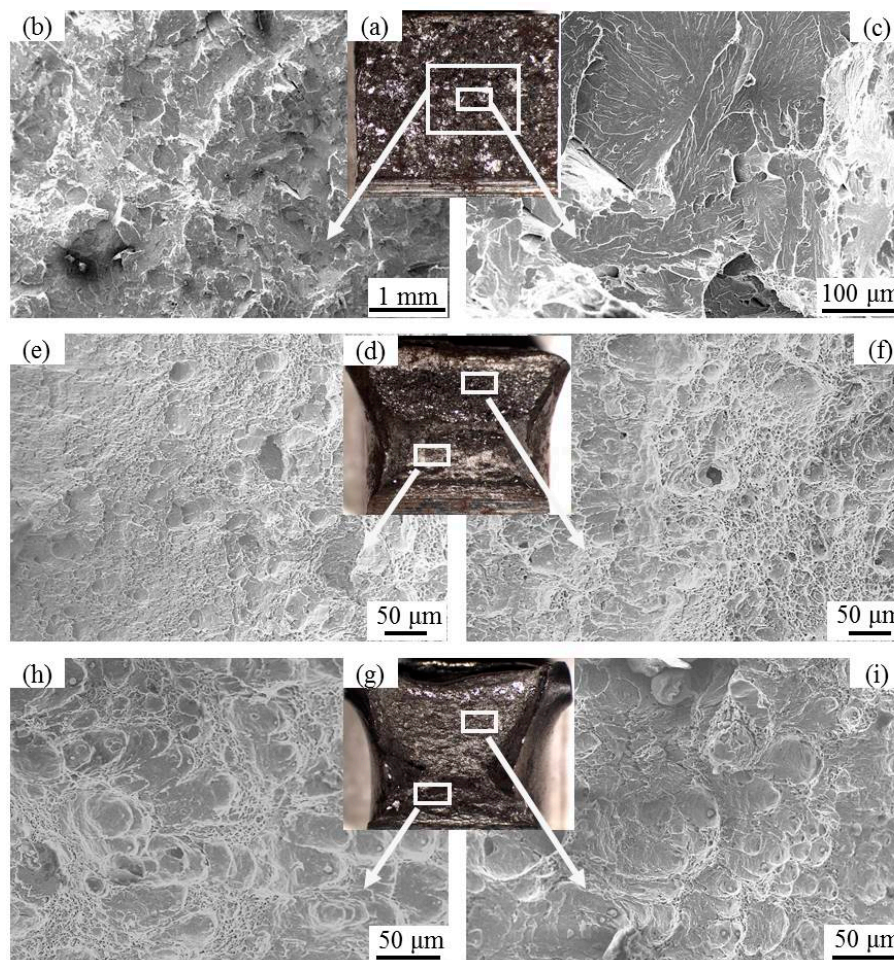

Figure 3. Macro fractographs and SEM images of fracture surfaces of HAZs: (**a**–**c**) A; (**d**–**f**) C11; (**g**–**i**) C27.

3.2. Typical Inclusions

The morphologies and mapping analysis results analyzed by SEM-EDS for typical inclusions in steel samples A, C11 and C27 are presented in Figures 4–6, respectively. Generally, complex inclusions comprising central oxides and peripheral sulfides are in the shape of globular or nearly globular.
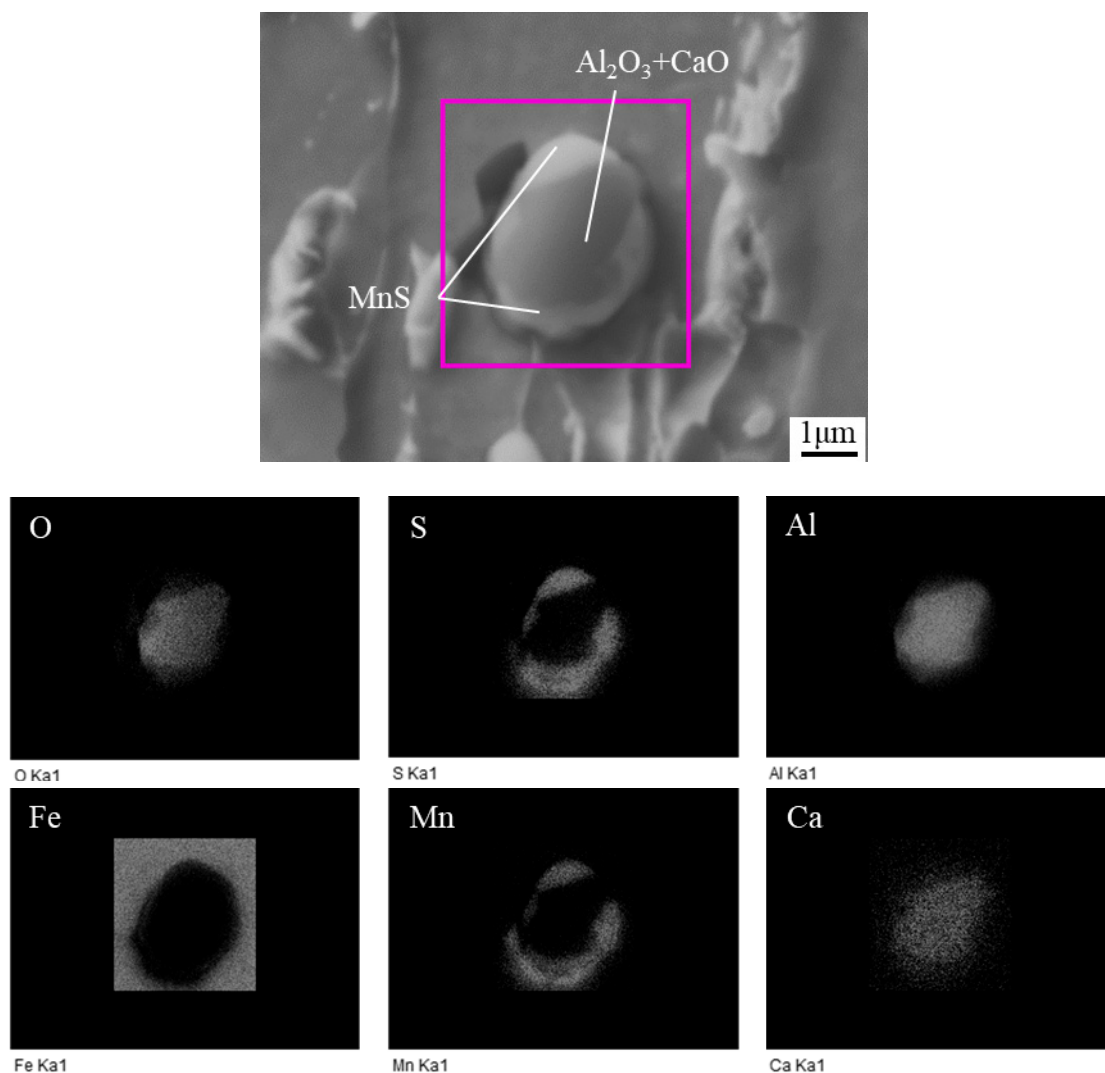

Figure 4. Elemental mapping pattern of typical inclusion in steel sample A.

The mapping analysis results of the typical inclusion in the conventional Al-killed steel sample A is shown in Figure 4. It is observed that the distributions of Ca and Al elements are both overlapped with O element. Meanwhile, the distribution of S element coincides with that of Mn element. It is indicated that the central part of the typical inclusion in steel sample A is composed of Al_2O_3 with a little CaO, denoted as Al_2O_3 + CaO. Besides, the sulfide covering the typical inclusion is MnS phase.

Figure 5 shows the distribution of Ca is not overlapped with O element but S and Mn elements. It is indicated the sulfide should be the solution of MnS phase and CaS phase, termed as (Ca, Mn)S. Meanwhile, in the central part of this inclusion, the distribution of Al element coincides with that of O element. Thus, the typical inclusion in steel sample C11 is mainly composed of irregular Al_2O_3 in the center with (Ca, Mn)S outside, as shown in Figure 5. It is observed that there are small amount of TiN locating at the edge of the typical inclusion in steel sample C11.
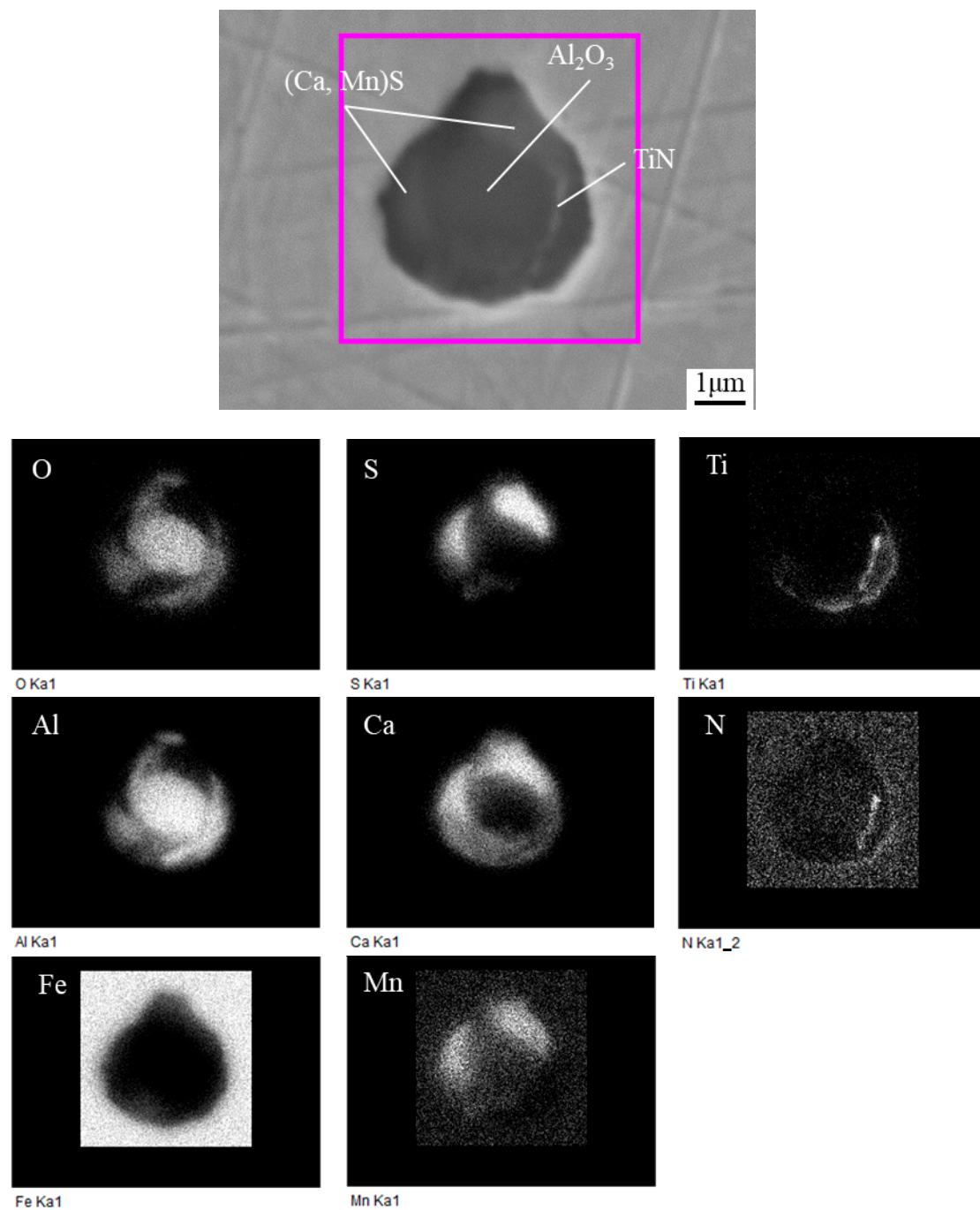
Figure 5. Elemental mapping pattern of typical inclusion in steel sample C11.

As shown in Figure 6, the typical inclusion in steel sample C27 containing 27 ppm Ca reveals a nearly globular shape. The distribution of Ca element is also not overlapped with O element but S element. Meanwhile, Mn element is detected in this inclusion. It is indicated that the sulfide is mainly composed of CaS phase with MnS phase. Therefore, the typical inclusion in steel sample C27 is mainly composed of central Al_2O_3 and peripheral (Ca, Mn)S, along with a small amount of TiN observed at the edge.
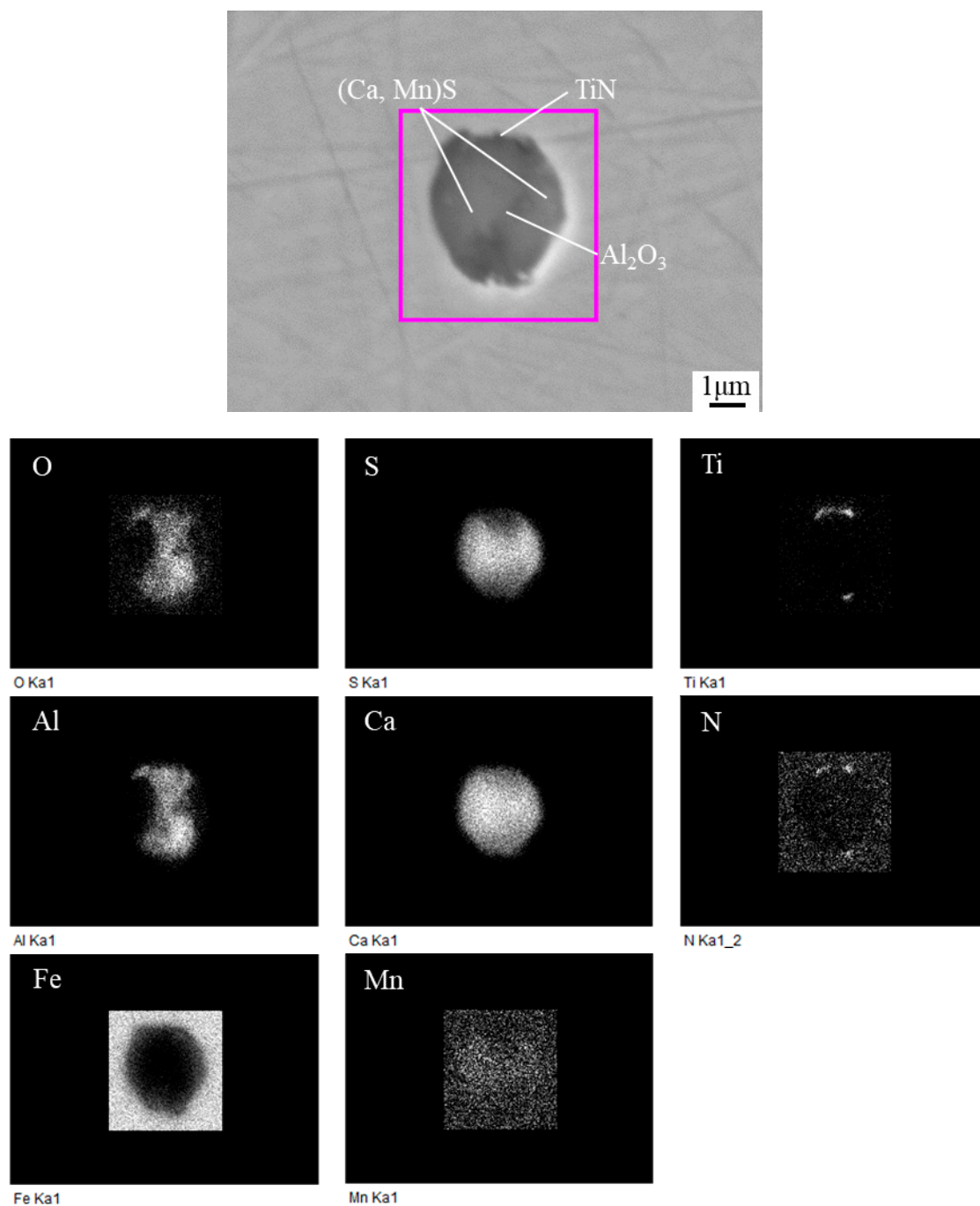
Figure 6. Elemental mapping pattern of typical inclusion in steel sample C27.

3.3. Number Density and Size of Inclusions

The analysis results of inclusions for steel samples A, C11 and C27 as shown from Figures 7–10 are based on the examination of inclusions in HAZs through IAAS. The numbers of inclusions examined in steel samples A, C11 and C27 are 2340, 1892 and 2762 in the observed areas of 69.5, 45.2 and 61.4 mm^2, respectively.

Figure 7 shows the relationship between Ca content in steel and the average size and number density of inclusions with the size larger than 1 μm in HAZs. With increasing the Ca content in steel from 5 to 11 and then to 27 ppm, the number density of inclusions is increased steadily from 33.7 to 41.9 and then to 45.0 mm^{-2} and the standard deviation is 34.09. Meanwhile, the average size of inclusions is decreased from 2.23 to 2.20 and then to 1.46 μm and the standard deviation is 0.19.
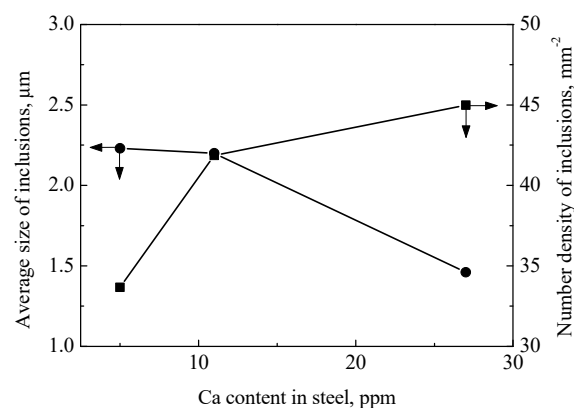
Figure 7. Changes in number density and average size of inclusions in different steels.

Figure 8 gives the size distributions of inclusions in steels with different Ca contents. It is seen that there are few inclusions larger than 10 µm in all three steel samples, and most of inclusions are smaller than 3 µm after Ca deoxidation. The frequencies of inclusions with size between 1 and 2 µm in A, C11 and C27 are 57.2%, 52.2% and 91.4%, respectively, suggesting that the average size of inclusions in steel sample C27 is much smaller than that in steel samples A and C11. The size distribution of steel sample A is similar with that of steel sample C11. Therefore, the average sizes of inclusions in steel samples A and C11 are at the same level, 2.23 and 2.20 µm, respectively, as shown in Figure 7.
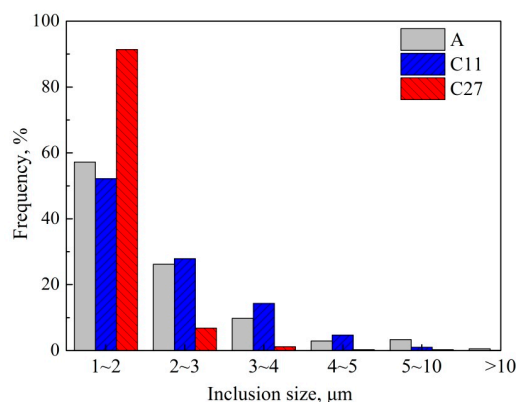

Figure 8. Size distributions of inclusions in the experimental steels.

3.4. Composition of Inclusions

Figure 9 shows the changes of average compositions of inclusions in steel samples A, C11 and C27, respectively. The Ca content in the average composition of inclusions gradually increases from 1.01% to 11.61% and then to 22.09% (in mass percentage) with increasing Ca content from 5 to 11 and then to 27 ppm. There is a similar tendency in the change of Al content in the average composition of inclusions, which increases from 16.54% to 21.95% and then to 25.22%. It is also noted that the Ti contents in the average composition of inclusions in both steel samples with Ca deoxidation, C11 and C27, 3.43% and 5.62%, are much higher than that in the conventional Al-killed steel sample A, 0.94%. As shown in Figures 5 and 6, the Ti element in inclusions existed in the form of TiN precipitate. It is inferred that the precipitation of TiN is promoted by Ca deoxidation. Figure 9 also shows that the content of S element in inclusions is relatively high, nearly more than 20%, but without significant change of S content in inclusions with increasing the Ca content. Besides, the Mn content in inclusions decreases sharply from 39.73% to 20.27% and then to 7.12% with addition of Ca content in steel from 5 to 11 and then to 27 ppm.
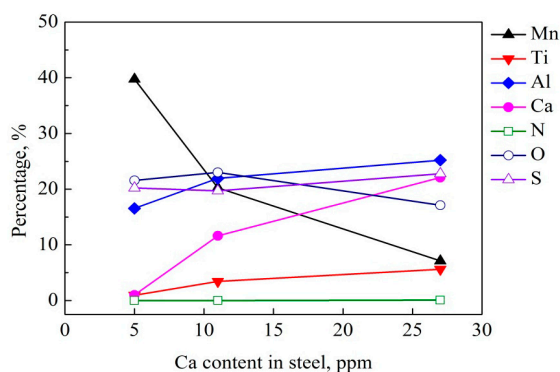
Figure 9. Changes of average composition of inclusions with Ca content in steel.

It is seen from Figures 4–6 that these typical inclusions in all three steel samples are complex inclusions composed of central oxides, outside sulfide and TiN at the edge. The complex inclusions could be classified into nine types [14] by the major compositional elements (Al, Ca, Ti, Mn, O, N and S) as shown in Figure 10. These nine types of inclusions are (1) Al_2O_3, (2) Al_2O_3 + CaO, (3) Al_2O_3 + MnS, (4) Al_2O_3 + CaO + MnS, (5) Al_2O_3 + CaS + MnS + TiN, (6) CaS + MnS + TiN, (7) MnS, (8) TiN, and (9) MnS + TiN. As shown in Figure 10, the frequencies of Al_2O_3 + CaS + MnS + TiN complex inclusions in steel samples C11 and C27 are as high as 88.74% and 68.28%, respectively. Therefore, Al_2O_3 + CaS + MnS + TiN complex inclusion is the main inclusion type in both steel samples with Ca deoxidation. In comparison, this type of inclusion is hardly found in steel sample A, but instead the main inclusions in steel sample A are MnS and Al_2O_3 + MnS with the frequencies of 35.84% and 27.96%, respectively. There are also small amounts of Al_2O_3 + CaO and Al_2O_3 + CaO + MnS complex inclusions in steel sample A with the frequencies of 5.79% and 12.49% respectively. It is concluded that the Ca element in the inclusions of steel sample A exist in the form of CaO in the Al_2O_3 + CaO or Al_2O_3 + CaO + MnS complex inclusions, as shown in Figure 4. However, the existent forms of Ca element in the inclusions of steel samples C11 and C27 are both CaS, as shown in Figures 5 and 6. It is also found, in Figure 10, that the frequencies of isolate MnS decreases from 35.84% to 8.4% and then to 1.92% with increasing Ca content in steel from 5 ppm to 11 ppm and then to 27 ppm. Meanwhile, the change of MnS + TiN inclusions frequency has the similar tendency, decreasing from 2.79% to 1.74% and then to 0.18%. The CaS + MnS + TiN type inclusion is hardly found in steels with Ca contents of 5 and 11 ppm, but the frequency of this type of inclusion increases up to 21.4% when the Ca content increases to 27 ppm, as shown in Figure 10.
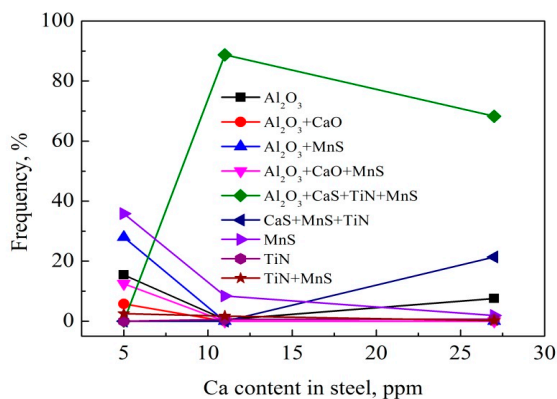

Figure 10. Variations of different types of inclusions with the increase of Ca content.

3.5. Characteristics of HAZ Microstructures

Figure 11 shows the typical HAZ microstructures of steel samples A, C11 and C27 after simulated welding with the heat input of 400 kJ·cm^{-1}. Grain boundary ferrites (GBFs) with network-like distribution are clearly observed in the HAZ microstructures of all three steel samples. Because GBFs form from the prior-austenite grain (PAG) boundaries and grow along them, the size of the cycle formed by GBF can indicate the size of PAG. The PAG sizes were measured by the straight intercept method of ASTM E112 standard. The intercept points per millimeter of three samples are 2.53, 3.65, 2.74, respectively, and the PAG sizes are deprived by the corresponding relation between the intercept point and the PAG sizes. The average PAG sizes of steel samples A, C11 and C27 are approximately 420, 260 and 390 μm, respectively. According to the result reported by Zhang et al. [15], austenite grain with the size larger than 200 μm was appropriate for the formation of IAF. As shown in Figure 11b, the intragranular part in the HAZ microstructure of steel sample A mainly consists of coarse ferrite side plates (FSPs), but it is quite different in both steel samples with Ca deoxidation, C11 and C27. In the steel samples C11 and C27, the intragranular part in the HAZ microstructure is mainly comprised of well-developed IAFs, as shown in Figure 11d,f.
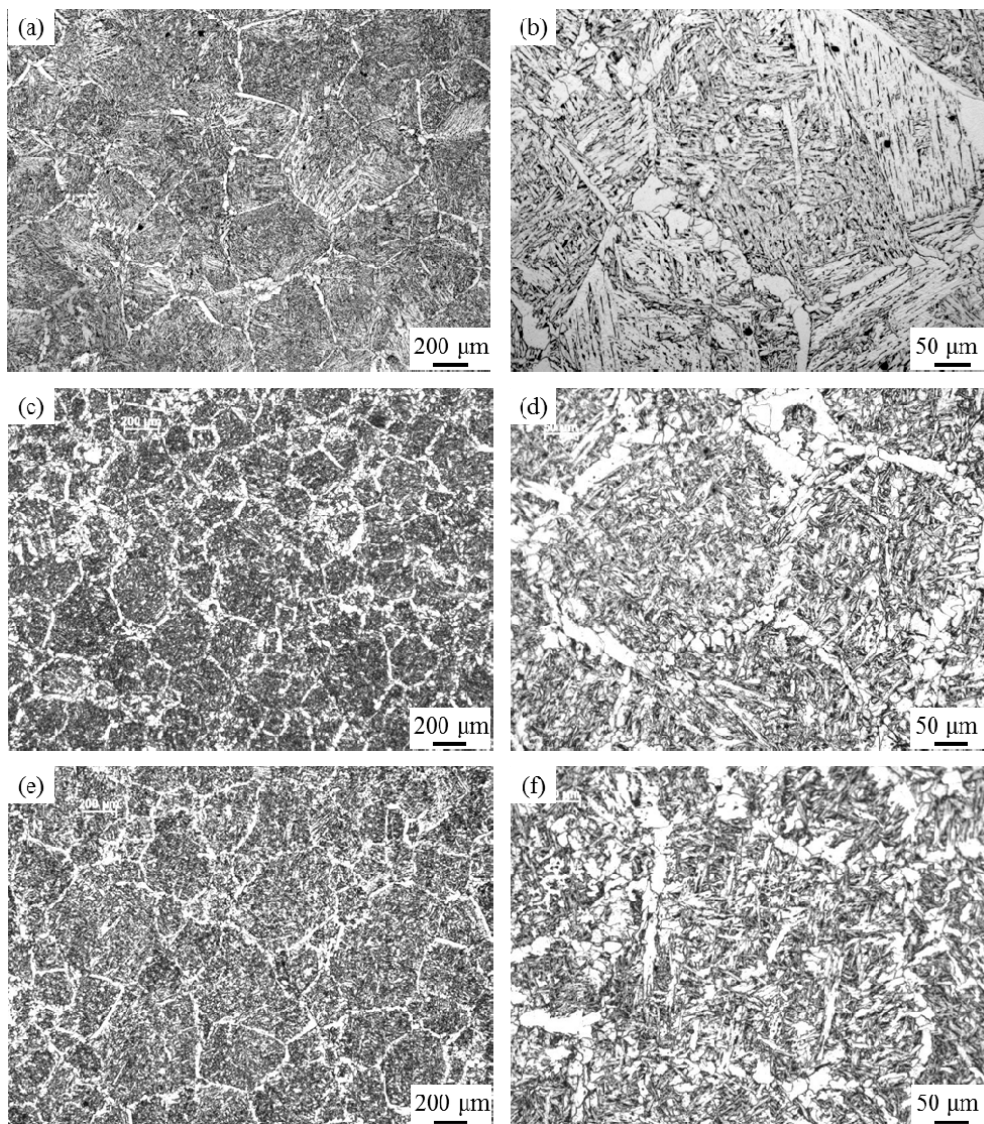

Figure 11. Typical HAZ microstructures for steel plates after simulated welding with heat input of 400 kJ·cm^{-1}: (**a**,**b**) A; (**c**,**d**) C11; (**e**,**f**) C27.

Figure 12 shows SEM micrographs of typical ferrite grains associated with inclusions in steel samples A, C11 and C27. As can be seen in Figure 12a, in steel sample A, the inclusion located in the coarse FSP lath is comprised of mainly Al_2O_3 + CaO and small amount of MnS. SEM-EDS analysis results shown in Figure 12d,f indicate that these inclusions in steel samples C11 and C27, inducing the formation of IAFs, are composed of Al_2O_3 + CaS + MnS + TiN.

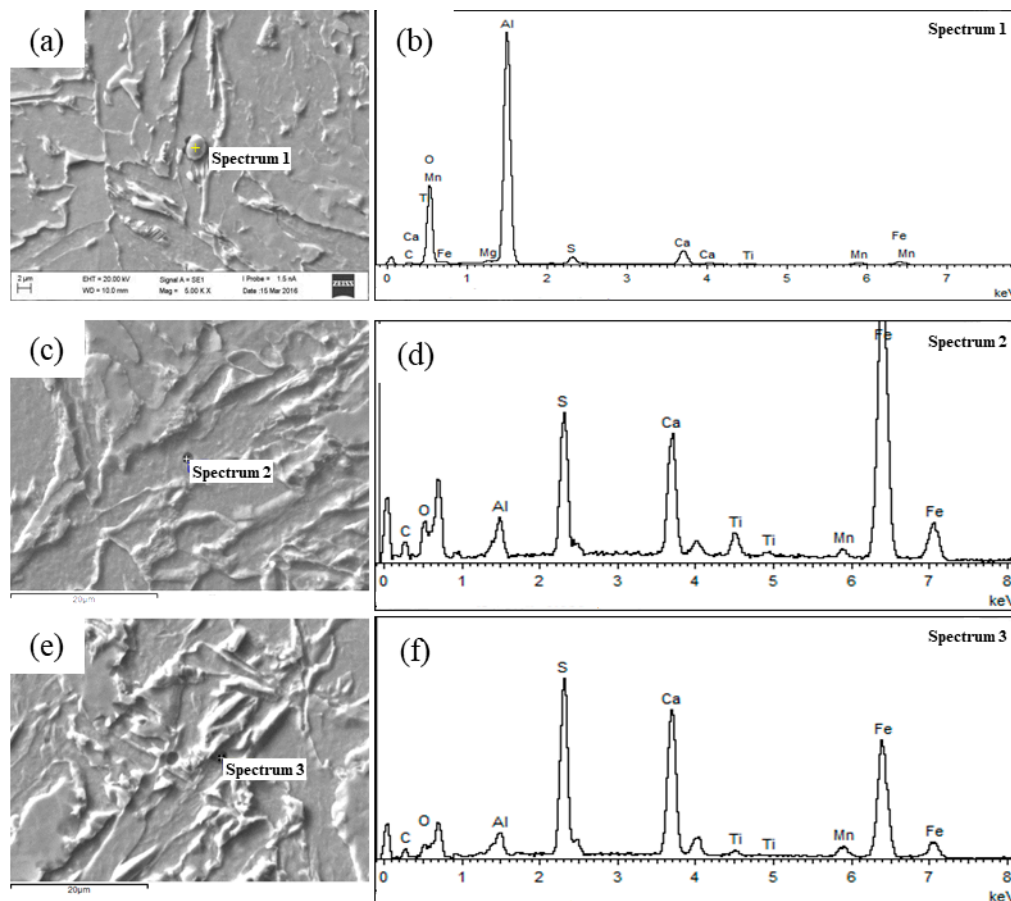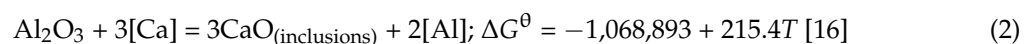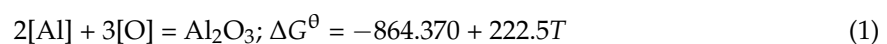**Figure 12.** EDS analysis results of inclusions in HAZs: (**a**,**b**) A, (**c**,**d**) C11, and (**e**,**f**) C27.

4. Discussion

4.1. Behavior of Ca Element in Oxide Metallurgy Technology

During the melting process of three samples A, C11 and C27, Ca was added into the melt after Al-deoxidation. The listed reactions would exist.

$$2[Al] + 3[O] = Al_2O_3; \Delta G^\theta = -864.370 + 222.5T \tag{1}$$

$$Al_2O_3 + 3[Ca] = 3CaO_{(inclusions)} + 2[Al]; \Delta G^\theta = -1{,}068{,}893 + 215.4T \, [16] \tag{2}$$
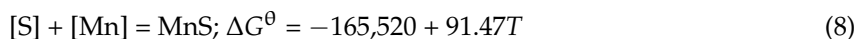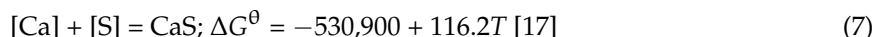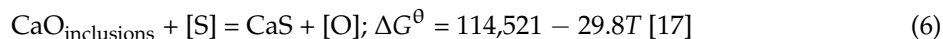
$$\lg f_i = \sum_{j=2}^{n} e_i^i [\%j] \tag{3}$$

$$\Delta G_r = \Delta G^\theta + RT\ln Q_r \tag{4}$$

Q_r is the reaction quotient which can be expressed as

$$Q_r = \frac{\alpha_{CaO \cdot Al_2O_3}}{\alpha_{Ca} \cdot \alpha_{Al} \cdot \alpha_O} \tag{5}$$

The ΔG_r have been calculated by Equation (2) [16]. The content of C, Si, Mn, Al, Ca are shown in Table 2. The coefficient activity has been calculated by Equation (3). If ΔG_r is negative, the reaction proceeds. If ΔG_r is positive, the reaction proceeds in the reverse direction.

The calculated results ΔG_r of reaction Equation (2) of three steels are $-153,275$ J·mol^{-1}, $-216,899$ J·mol^{-1}, $-249,188$ J·mol^{-1}, respectively. So, the reaction Equation (2) exist in A, C11 and C27 samples. During the process of reaction Equation (2), the products of Al deoxidation, Al_2O_3, are modified into complex oxide inclusions.

$$CaO_{inclusions} + [S] = CaS + [O]; \Delta G^{\theta} = 114,521 - 29.8T \text{ [17]} \tag{6}$$

$$[Ca] + [S] = CaS; \Delta G^{\theta} = -530,900 + 116.2T \text{ [17]} \tag{7}$$

$$[S] + [Mn] = MnS; \Delta G^{\theta} = -165,520 + 91.47T \tag{8}$$

During the reaction process, the formation of CaS and MnS are discussed. The reaction of S, Ca and Mn are shown as Equations (6)–(8). Figure 13a shows the change of Gibbs free energy of reaction with activity of CaO in CaO-Al_2O_3. As it can be seen, the Gibbs free energy is negative when α_{CaO} is greater than 0.03 and the CaO in CaO-Al_2O_3 change into CaS. The Gibbs free energy is positive when α_{CaO} is less than 0.03 and the CaO in CaO-Al_2O_3 does not change into CaS. The content of CaO in CaO-Al_2O_3 of three samples can be calculated approximately in Figure 9. They are 13%, 28.8%, 37.5% respectively. The activity of CaO in CaO-Al_2O_3 can be obtained by the calculated results of Yang [17] and the content of CaO in CaO-Al_2O_3 of three samples. The α_{CaO} is greater than 0.03 when the content of CaO is greater than 20%, therefore, the reaction of Equation (6) only exists in C11 and C27 samples.
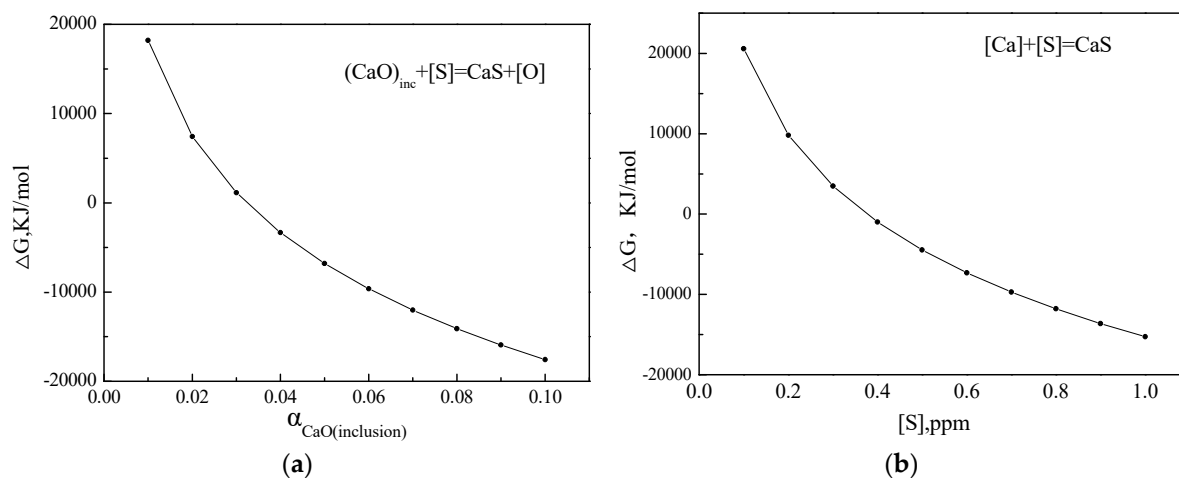

Figure 13. Change of Gibbs free energy of reaction with (**a**) activity of CaO in CaO-Al_2O_3 and (**b**) dissolved S.

There are two sources of CaS [17]. One is the reaction product of CaO in CaO·Al_2O_3 and S in steel expressed by Equation (6). The other is the product of dissolved Ca and S expressed by Equation (8). It is easier to form sulfide during the solidification and cooling processes. The solubility of sulfide is decreased greatly during the solidification and cooling process. So, the MnS formed on the Al_2O_3 and Al_2O_3 + CaO in Sample A by Equation (8).

Figure 13b shows the change of Gibbs free energy of reaction with content of dissolved S. The Gibbs free energy is positive when the content of dissolved S is less than 0.3 ppm and the reaction of Equation (6) proceeds in the reverse. In C11 and C27 samples, the content of dissolved S decrease because of the formation of MnS by Equation (7). So, the reaction of Equation (6) proceeds in reverse direction and decomposes to dissolved S when the content of dissolved S is less than 0.3 ppm. MnS forms continuously by the dissolved S and Mn. So, the major final inclusions are the type (4) in sample

A and type (5) in samples C11 and C27, as shown in Figure 10. In summary, the order of reactions in Sample A are Equations (1), (2) and (7). Al_2O_3 nucleated firstly in liquid steel, and then, MnS precipitated on Al_2O_3 after adding Ca. The order of reactions in samples C11 and C27 are Equations (1), (2), (4), (6) and (7); the main inclusion is type (5).

As shown in Figures 4–6, the Ti contents in both steel samples with Ca deoxidation, in C11 and C27, existed in the form of TiN, which precipitated on the surface of the complex inclusions. By comparison with Al and Ca in steel samples C11 and C27, the deoxidation ability of Ti is weaker. Meanwhile, the contents of oxygen in both steel samples are in a low level (less than 13 ppm). Therefore, TiN is promoted to precipitate on the surface of inclusions. as shown in Figure 10.

4.2. Mechanism of HAZ Toughness Improved by Ca Deoxidation

Oh et al. [17] reported that the austenite grain with the size larger than 100 μm was appropriate for the stable growth of GBF. As shown in Figure 11, sizes of PAGs in all three steel samples are larger than 200 μm, and thus, GBF is observed clearly in the HAZ microstructure. It has been reported that the austenite grain with size around 200 μm benefits the formation of IAF [6,16]. Moreover, Al_2O_3 + MnS inclusions in conventional LCAK steel plates are impotent to induce the nucleation of IAF during the process of high heat input welding with 400 kJ·cm^{-1} [6]. Accordingly, the intragranular part of coarse austenite grain was occupied by brittle HAZ microstructure, namely FSP, as shown in Figure 11b. As a consequence, the HAZ toughness of conventional Al-killed steel sample A was greatly deteriorated.

It is widely accepted that non-metallic inclusions in steel may act as effective nuclei for IAF. Many mechanisms of IAF nucleation on inclusions have been proposed, including (1) reduction of interfacial energy [18], (2) decrease in lattice mismatch [19,20], (3) lessening thermal strains around the inclusions [21,22], and (4) formation of solute depletion zone around the inclusions [23]. In present study, the majority of inclusions are Al_2O_3 + CaS + MnS + TiN complex inclusions, as shown in Figure 10. TiN is distributed at the edge of this type of complex inclusions, as shown in Figures 5 and 6. Kanazawa et al. [24] have reported that TiN particles may promote the formation of ferrite. Mu et al. [25] also confirmed that the TiN phase was an effective nucleation site for the formation of intragranular ferrite. The role of TiN in heterogeneous nucleation of IAF was evaluated by the lattice matching theory [21,26]. According to the literature, the lattice misfit between TiN substrate and ferrite was 3.8% [27]. It is supposed that the narrow TiN layer on the inclusion surface promotes acicular ferrite nucleation due to the low interface energy [21].

As discussed in Section 4.1, in samples C11 and C27, the CaS decomposes to dissolved S and the MnS forms continuously, so the type of inclusions contain (Ca, Mn)S, covering the central Al_2O_3, as shown in Figures 5 and 6 may arouse the formation of Mn-depleted zone (MDZ) around the interface between inclusion and steel matrix. MDZ is an important factor for inclusions to accelerate the nucleation of the IAF [28]. On the contrary, the Al_2O_3 + MnS inclusions in A steel does not deliver S from inside to outside, so the formation of MnS is not continuous. Additionally, most of inclusions in both steel samples C11 and C27 are of sizes between 1 and 3 μm, as shown in Figure 8. It has been reported that the inclusions with sizes around 2 μm could induce the formation of IAF [6,29–31]. In conclusion, it is inferred that the combined action of low lattice misfit and MDZ may be the mechanisms for the formation of well-developed IAF in HAZ during the high heat input welding and the main mechanism is that Mn-depleted zone (MDZ). As a result, excellent HAZ toughness of steel plates after high heat input welding is obtained by utilizing oxide metallurgy technology with Ca deoxidation.

5. Conclusions

The effect of Ca content on the number, size and composition of inclusions in the heat-affected zones (HAZs) of steel plates with Ca deoxidation was investigated based on the experimental study. The HAZ toughness was also measured after simulating welding process with the high heat input of 400 kJ·cm^{-1}. The following conclusions were drawn:

1. The typical inclusions found in the HAZs of steel samples with Ca deoxidation containing 11 and 27 ppm Ca were Al_2O_3 + CaS + MnS + TiN complex inclusions with the size in the range of 1~3 μm, together with TiN formed at the edge of this type of inclusions.
2. In conventional Al-killed steel sample containing 5 ppm Ca, the existence form of Ca element was CaO in the Al_2O_3 + CaO or Al_2O_3 + CaO + MnS complex inclusions. On the other hand, the Ca element in the inclusions of the steels with Ca deoxidation mainly existed in the form of (Ca, Mn)S covering the central Al_2O_3.
3. With increasing Ca content in the steels from 5 to 11 and 27 ppm, the size of inclusions increased from 2.23 to 2.20 and then to 1.46 μm, and the number density of inclusions increased steadily from 33.7 to 41.9, and then to 45.0 mm^{-2}.
4. The average size of prior-austenite grains in HAZs of conventional Al-killed deoxidation and developed steel with Ca deoxidation were all larger than 200 μm. In the steel sample with Ca deoxidation, Al_2O_3 + CaS + MnS + TiN complex inclusions were potent to induce the formation of intragranular acicular ferrite (IAF) so that well-developed IAF formed in the HAZ microstructures. Therefore, excellent HAZ toughness of steel plates after welding with heat input of 400 $kJ \cdot cm^{-1}$ was obtained by utilizing oxide metallurgy technology with Ca deoxidation.

Conflicts of Interest: The authors declare no conflict of interest.

References

1. Yang, J.; Zhu, K.; Wang, R.; Shen, J.G. Improving the toughness of heat affected zone of steel plate by use of fine inclusion particles. *Steel Res. Int.* **2011**, *82*, 552–556. [CrossRef]
2. Yang, J.; Zhu, K.; Wang, G.D. Progress in the technological development of oxide metallurgy for manufacturing steel plates with excellent HAZ toughness. *Baosteel Tech. Res.* **2008**, *2*, 43–50.
3. Ogibayashi, S. Advances in technology of oxide metallurgy. *Nippon Steel Tech. Rep.* **1994**, 70–76.
4. Xu, L.Y.; Yang, J.; Wang, R.Z.; Wang, Y.N.; Wang, W.L. Effect of Mg content on the microstructure and toughness of heat-affected zone of steel plate after high heat input welding. *Metall. Mater. Trans. A* **2016**, *47*, 3354–3364. [CrossRef]
5. Zhu, K.; Yang, Z.G. Effect of magnesium on the austenite grain growth of the heat-affected zone in low-carbon high-strength steels. *Metall. Mater. Trans. A* **2011**, *42*, 2207–2213. [CrossRef]
6. Xu, L.Y.; Yang, J.; Wang, R.Z.; Wang, W.L.; Wang, Y.N. Effect of Mg addition on formation of intragranular acicular ferrite in heat-affected zone of steel plate after high-heat-input welding. *J. Iron Steel Res. Int.* **2018**, *25*, 433–441. [CrossRef]
7. Shi, M.H.; Zhang, P.Y.; Wang, C.; Zhu, F.X. Effect of high heat input on toughness and microstructure of coarse grain heat affected zone in Zr bearing low varbon steel. *ISIJ Int.* **2014**, *54*, 932–937. [CrossRef]
8. Kojima, A.; Kiyose, A.; Uemori, R.; Minagawa, M.; Hoshino, M.; Nakashima, T.; Ishida, K.; Yasui, H. Super high HAZ toughness technology with fine microstructure imparted by fine particles. *Nippon Steel Tech. Rep.* **2004**, *90*, 2–6.
9. Abraham, S.; Bodnar, R.; Raines, J.; Wang, Y.F. Inclusion engineering and metallurgy of calcium treatment. *J. Iron Steel Res. Int.* **2018**, *25*, 133–145. [CrossRef]
10. Yang, S.F.; Li, J.S.; Wang, Z.F.; Li, J.; Lin, L. Modification of MgO·Al_2O_3 spinel inclusions in Al-killed steel by Ca-treatment. *Int. J. Min. Met. Mater.* **2011**, *18*, 18–23. [CrossRef]
11. Yang, D.; Wang, X.H.; Yang, G.W.; Wei, P.Y.; He, J.P. Inclusion evolution and estimation during secondary refining in calcium treated aluminum killed steels. *Steel Res. Int.* **2014**, *85*, 1517–1524. [CrossRef]
12. Ren, Y.; Zhang, Y.; Zhang, L. A kinetic model for Ca treatment of Al-killed steels using FactSage macro processing. *Ironmak. Steelmak.* **2017**, *44*, 497–504. [CrossRef]

13. Liu, Y.; Zhang, L.F.; Zhang, Y.; Duan, H.J.; Ren, Y.; Yang, W. Effect of sulfur in steel on transient evolution of inclusions during calcium treatment. *Metall. Mater. Trans. B* **2018**, *49*, 610–626. [CrossRef]

14. Wang, Y.N.; Yang, J.; Xin, X.L.; Wang, R.Z.; Xu, L.Y. The effect of cooling conditions on the evolution of non-metallic inclusions in high manganese TWIP steels. *Metall. Mater. Trans. B* **2016**, *47*, 1378–1389. [CrossRef]

15. Zhang, D.; Terasaki, H.; Komizo, Y. In situ observation of the formation of intragranular acicular ferrite at non-metallic inclusions in C-Mn steel. *Acta Mater.* **2010**, *58*, 1369–1378. [CrossRef]

16. Yang, G.W.; Wang, X.H. Inclusion evolution after calcium addition in low carbon Al-killed steel with ultra low sulfur content. *ISIJ Int.* **2015**, *55*, 126–133. [CrossRef]

17. Oh, Y.J.; Lee, S.Y.; Byun, J.S.; Shim, J.H.; Cho, Y.W. Non-metallic inclusions and acicular ferrite in low carbon steel. *Mater. Trans.* **2000**, *41*, 1663–1669. [CrossRef]

18. Ricks, R.A.; Howell, P.R.; Barritte, G.S. The nature of acicular ferrite in HSLA steel weld metals. *J. Mater. Sci.* **1982**, *17*, 732–740. [CrossRef]

19. Gregg, J.M.; Bhadeshia, H.K.D.H. Titanium-rich mineral phases and the nucleation of bainite. *Metall. Mater. Trans. A* **1994**, *25*, 1603–1611. [CrossRef]

20. Enomoto, M. Nucleation of phase transformations at intragranular inclusions in steel. *Met. Mater.* **1998**, *4*, 115–123. [CrossRef]

21. Yamada, T.; Terasaki, H.; Komizo, Y. Relation between inclusion surface and acicular ferrite in low carbon low alloy steel weld. *ISIJ Int.* **2009**, *49*, 1059–1062. [CrossRef]

22. Nako, H.; Okazaki, Y.; Speer, J.G. Acicular ferrite formation on Ti-rare earth metal-Zr complex oxides. *ISIJ Int.* **2015**, *55*, 250–256. [CrossRef]

23. Shim, J.H.; Cho, Y.W.; Chung, S.H.; Shim, J.D.; Lee, D.N. Nucleation of intragranular ferrite at Ti_2O_3 particle in low carbon steel. *Acta Mater.* **1999**, *47*, 2751–2760. [CrossRef]

24. Kanazawa, S.; Nakashima, A.; Okamoto, K.; Kanaya, K. Improved toughness of weld fussion zone by fine TiN particles and development of a steel for large heat input welding. *Tetsu-to-Hagané* **1975**, *11*, 2589–2603. [CrossRef]

25. Mu, W.Z.; Jönsson, P.G.; Shibata, H.; Nakajima, K. Inclusion and microstructure characteristics in steels with TiN additions. *Steel Res. Int.* **2016**, *87*, 339–348. [CrossRef]

26. Bramfitt, B.I. The effect of carbide and nitride additions on the heterogeneous nucleation behavior of liquid iron. *Metall. Trans.* **1970**, *1*, 1987–1995. [CrossRef]

27. Ohkita, S.; Horii, Y. Recent development in controlling the microstructure and properties of low alloy steel weld metals. *ISIJ Int.* **1995**, *35*, 1170–1182. [CrossRef]

28. Mabuchi, H.; Uemori, R.; Fujioka, M. The role of Mn depletion in intra-granular ferrite transformation in the heat affected zone of welded joints with large heat input in structural steels. *ISIJ Int.* **1996**, *36*, 1406–1412. [CrossRef]

29. Chai, F.; Yang, C.F.; Su, H.; Zhang, Y.Q.; Xu, Z. Effect of magnesium on inclusion formation in Ti-killed steels and microstructural evolution in welding induced coarse-grained heat affected zone. *J. Iron Steel Res. Int.* **2009**, *16*, 69–74. [CrossRef]

30. Wen, B.; Song, B.; Pan, N.; Hu, Q.Y.; Mao, J.H. Effect of SiMg alloy on inclusions and microstructhres of 16Mn steel. *Ironmak. Steelmak.* **2011**, *38*, 577–583. [CrossRef]

31. Zheng, C.C.; Wang, X.M.; Li, S.R.; Shang, C.J.; He, X.L. Effects of inclusions on microstructure and properties of heat-affected-zone for low-carbon steels. *Sci. China Technol. Sci.* **2012**, *55*, 1556–1565. [CrossRef]